Copper Phosphinate Complexes as Molecular Precursors for Ethanol Dehydrogenation Catalysts

Tomas Pokorny[#], Iaroslav Doroshenko[#], Petr Machac, Lucie Simonikova, Zdenek Moravec, Jiri Pinkas, and Ales Styskalik*

Department of Chemistry, Faculty of Science, Masaryk University, Kotlarska 2, CZ-61137 Brno, Czech Republic

* Corresponding author. Tel.: +420549498702
E-mail: styskalik@chemi.muni.cz (A. Styskalik).

[#] Tomas Pokorny and Iaroslav Doroshenko contributed equally to this work and should be considered co-first authors.

Abstract

Nowadays, the production of acetaldehyde heavily relies on the petroleum industry. Developing new catalysts for the ethanol dehydrogenation process, which could sustainably substitute current acetaldehyde production methods, is highly desired. Among ethanol dehydrogenation catalysts, copper-based materials have been intensively studied. Unfortunately, the Cu-based catalysts suffer from sintering and coking, which lead to rapid deactivation with time-on-stream (TOS). Phosphorus doping has been demonstrated to diminish coking in methanol dehydrogenation, fluid catalytic cracking, and ethanol-to-olefin reactions. This work reports a pioneering application of the well-characterized copper phosphinate complexes as molecular precursors for copper-based ethanol dehydrogenation catalysts enriched with phosphate groups (**Cu-phosphate/SiO$_2$**). Three new catalysts (**CuP-1**, **CuP-2**, **CuP-3**), prepared by the deposition of complexes {Cu(SAAP)}$_n$ (**1**), [Cu$_6$(BSAAP)$_6$] (**2**), and [Cu$_3$(NAAP)$_3$] (**3**) on the surface of commercial SiO$_2$, calcination at 500 °C, and reduction in the stream of the forming gas 5% H$_2$/N$_2$ at 400 °C exhibited unusual properties. First, the catalysts showed a rapid increase in catalytic activity. After reaching a maximum conversion, the catalyst started to deactivate. The unusual behavior could be explained by the presence of the phosphate phase, which prevented the Cu^{2+} reduction. The phosphorus content gradually decreased during time-on-stream, copper was reduced, and the activity increased. The deactivation of the catalyst could be related to the copper diffusion processes. The most active **CuP-1** catalyst reaches a maximum of 74 % ethanol conversion and over 98 % acetaldehyde selectivity at 325 °C and WHSV = 2.37 h^{-1}.

1

1 Introduction

Nowadays, the production of chemical compounds tends to focus on ecology and sustainability.[1,2] Acetaldehyde is a large-scale substance produced worldwide for many applications and as a precursor for further synthesis (acetic acid, ethyl acetate).[3] Current production of acetaldehyde is mainly based on petroleum chemistry.[4–8] First, the ethylene is produced by energetically demanding steam cracking, and then the acetaldehyde is made by the Wacker oxidation using a homogeneous catalyst containing heavy metals.[9,10] Non-oxidative dehydrogenation of ethanol to acetaldehyde (the first step of the Lebedev process[11,12]) shows the utilization of bio-ethanol to produce a variety of sustainable and bio-based chemicals.[13,14]

According to the literature reports, copper acts as a highly active and selective ethanol dehydrogenation catalyst.[7] For example, high selectivity to acetaldehyde (up to 100 %) has been reported by Chang et al., where rice husk ash (more than 99 % SiO_2) with copper nanoparticles (1—1.5 nm) were used as catalysts.[15] However, current copper-based catalysts suffer from deactivation by coking and sintering.[14,16–19] Coking has been shown to be one of the deactivation processes in Cu/SiO_2 catalysts prepared by dry impregnation, strong electrostatic adsorption, hydrolytic sol-gel, and solvothermal hot injection.[20] Similarly, Pampararo et al. showed a carbon deposition on Cu/SiO_2 catalysts prepared by aerosol-assisted sol-gel. The more active the catalysts, the higher amount of carbonaceous materials deposited during the catalytic reaction.[21] In addition to catalyst coking, copper sintering presents a severe problem at higher temperatures. For example, Cu/SiO_2 catalysts prepared by incipient wetness impregnation lost half of their activity during 4 hours at 300 °C. The deactivation was caused by Cu sintering.[22] Similarly, Cu/SiO_2 samples with 0.5 and 1 wt% of copper started losing catalytic activity at 300 °C due to the particle sintering. Surprisingly, smaller particles prepared by the deposition-precipitation method (23 nm) exhibited better catalytic activity and stability than larger particles prepared by wet impregnation (84 nm).[16] These results suggest that it is crucial to study the stability of copper-based catalysts, describe the sintering and coking in detail, and develop new catalysts based on the gained knowledge.[14,16–19]

Applying molecular precursors to prepare structure-controlled catalysts with homogeneously dispersed catalytic species on the support is a well-known and widely used method.[23–25] However, there is a lack of information on applying phosphorus-containing metal complexes (phosphates, phosphonates, and phosphinates) as precursors to non-oxidative ethanol dehydrogenation catalysts. The addition of phosphorus into Cu/SiO_2 catalysts prepared by incipient wetness impregnation and ion-exchange method was studied by Yamamoto et al.[26] Interestingly, phosphorus-containing catalysts exhibited a significant increase in formaldehyde productivity in methanol dehydrogenation. Incorporating phosphorus in Cu/AlPO catalysts is known to influence the catalytic activity and stability.[27] Synthesizing alumina modified with phosphorus reduces the amount of coke formation in the methanol-to-dimethyl ether dehydration reaction.[28] Similarly, the addition of phosphorus has been reported to lead to a decrease in coke formation in hydrocarbon catalysis and consequently to increased catalytic lifetime.[26] Bij et al.[29] and Xia et al.[30] pointed to anti-coking properties of phosphorus-doped zeolites.

2

This work presents the structures of new copper phosphinate complexes of various nuclearity, their deposition on porous silica support by wet impregnation followed by thermal decomposition leading to **Cu-phosphate/SiO₂** materials, and the catalytic properties of these catalysts in ethanol dehydrogenation. The main goal of the application of the copper phosphinate complexes in wet impregnation was to disperse copper and phosphorus homogeneously on the surface of the SiO₂ matrix. Small and uniform particles containing both Cu and P were successfully formed. Interestingly, the materials prepared in such a way exhibited a peculiar catalytic behavior, distinctively different from the benchmark catalyst obtained by the dry impregnation method. The most active **Cu-phosphate/SiO₂** catalyst was analyzed ex-situ by numerous characterization techniques at the different stages of the catalyst lifetime (i.e., after calcination, after H_2 treatment, at the top of catalytic activity, spent catalyst) to gain a deep understanding of the unprecedented catalytic properties.

2 Experimental part

2.1 General procedures

All reactions were performed using general synthetic techniques; no special conditions were used. Commercially available benzyl carbamate (TCI), dichlorophenylphosphine (Sigma), NaOH, salicylaldehyde (Sigma), 5-bromosalicylaldehyde (Sigma), 2-hydroxy-1-naphtalaldehyde (Sigma), methanol-d_4 (Sigma), propan-2-ol (p.a.), ethanol (p.a.), methanol (p.a.), acetone (p.a.), pentane (p.a.), acetic acid (p.a.), $Cu(NO_3)_2 \cdot 2.5H_2O$, Aerosil 300 (Evonik) were used as received.

2.2 Characterization methods

Elemental maps, nanoparticles size, and distribution were measured by scanning transmission electron microscopy with energy dispersive X-ray spectroscopy (STEM-EDS) on a Thermo Fisher Scientific Talos F200 instrument equipped with a Bruker X-flash EDS detector. The device operated at 40—200 kV of accelerating potential. The size of the nanoparticles was determined using an ImageJ image processing program.[31] Nanoparticle diameters were measured across the widest side. The surface chemical composition was analyzed by X-ray photoelectron spectroscopy (XPS) on a Kratos Axis Supra device equipped with a monochromatic X-ray source with Al K_α (E = 1486.6 eV) excitation. Binding energy 284.8 eV for C1s was used for calibration. An Autosorb iQ3 (Quantachrome Instrument) porosimeter was used for measuring specific surface area by nitrogen adsorption. Both isotherms (adsorption and desorption) were measured at the liquid nitrogen temperature (−195.7 °C). Before measurements, samples were degassed at the temperature of 200 °C. BET analysis was used to determine the specific surface area from isotherms measured in the 0.05—0.30 relative pressure range. A Netsch STA 449 Jupiter instrument was used for thermogravimetric (TG) analyses. Samples were heated to 1000 °C in Pt crucibles with a heating rate of 5 °C min^{-1} in a synthetic air atmosphere with a flow of 100 cm^3 min^{-1}. Single-crystal X-ray diffraction measurements were performed on a Rigaku diffraction system (MicroMax007HF DW rotating anode source with multilayer optic, partial χ axis goniometer, Saturn 724+ HG detector, and Cryostream cooling device). The Mo-K$_\alpha$ (λ = 0.7107 Å) radiation was used. Data were corrected for Lorentz and polarization effects; absorption was taken into account on a semi-empirical basis using multiple-scans.[32–34] *CrystalClear* (Rigaku 2014) and *CrysAlisPro* (Agilent

Technologies 2013) software packages were used for data collection and reduction. The structures were solved using *SHELXT*[35] program and refined (full matrix least-squares refinement on F_o^2) using *SHELXL*[36] program. An EMPYREAN instrument by PANalytical was used for powder X-ray diffraction analyses. Samples were placed on a spinning sample bed. The Co K_α radiation (λ = 1.78901 Å) was used (20 mA, 30 KV). A semiconductor detector was used in a 1D mode. Elemental contents were measured by inductively coupled plasma optical emission spectroscopy (ICP-OES). ICP-OES analyses were done on an ICP-OES spectrometer iCAP PRO (Thermo, RF Power 1.10 kW, nebulizer gas flow 0.65 dm^3 min^{-1}, radial viewing high 11.0 mm). Emission lines 177.495, 178.284, and 213.618 nm for P and 324.754, and 327.396 nm for Cu were used. IR spectra were recorded on a Bruker Tensor 27 FTIR spectrometer with a Bruker Platinum ATR system. The solution NMR spectra were recorded on a Bruker AvanceIII 300 NMR spectrometer at frequencies 300.1 MHz for ^{1}H and 121.5 MHz for ^{31}P in 5 mm NMR tubes. CD$_3$OD was used as an internal lock. The spectra were referenced to the residual proton signal of CHD$_2$OD (3.33 ppm), while the ^{31}P spectra were referenced to 85 % H$_3$PO$_4$ (0 ppm).

2.3 Ligand and complex synthesis

Detailed synthetic procedures of (2-{[(E)-(2-hydroxyphenyl)methylidene]amino}propan-2-yl)phenylphosphinate (HSAAP⁻), (2-{[(E)-(5-bromo-2-hydroxyphenyl)methylidene]amino}propan-2-yl)phenylphosphinate (HBSAAP⁻), and (2-{[(E)-(2-hydroxynaphthalen-1-yl)methylidene]amino}propan-2-yl)phenylphosphinate (HNAAP⁻) sodium salts (Figure 1) are described in Supplementary Materials. Ligands HSAAP⁻, HBSAAP⁻, and HNAAP⁻ were deprotonated and used to prepare copper phosphinate complexes {Cu(SAAP)}$_n$, (**1**), [Cu$_6$(BSAAP)$_6$] (**2**), and [Cu$_3$(NAAP)$_3$] (**3**). Synthesis details and characterization are described in Supplementary Materials (Table S1—S3). Copper phosphinate complexes **1—3** were used as precursors for the catalyst preparation (see below).

2.4 Catalyst preparation

CuP-1—3 catalysts were prepared by the wet impregnation of the corresponding complex **1—3** on the commercial SiO$_2$ support (Aerosil 300) from MeOH solution (50 cm^3). After adding Aerosil to a clear solution of a complex, the suspension was sonicated for 5 min for homogenization and then evaporated on a rotary evaporator. The well-dried homogeneously green sample was calcined in air for 10 h at 500 °C, resulting in a light-blue product. The weight of the complex and support was calculated to obtain 2.5 wt% Cu loading (masses used in the preparation are summarized in Table S4). **Cu-DI** benchmark catalyst was prepared by the previously reported procedure.[20] Cu(NO$_3$)$_2$·2.5H$_2$O (91.5 mg, 0.393 mmol) was dissolved in water (10 cm^3) and mixed with silica (Aerosil 300, 1.0 g) to form a paste. The sample was dried in an oven at 70 °C with occasional mixing. The dried catalyst was ground and calcined at 500 °C for 5 hours.

2.5 Catalytic reactor details

For catalysis, a fix-bed catalytic reactor was used. Gas chromatography with a flame ionization detector was connected to determine the catalytic activity. Catalytic tests were performed at 325 °C for up to 50 h. The effluent gas analysis was carried out by an HP 6890 Gas

Chromatograph equipped with a flame ionization detector (FID) and a Thermo scientific TG-BOND U column (length of 30 m, internal diameter of 0.32 mm, film thickness of 10 μm). Calcined catalysts (200 mg) with selected grain size (0.2—0.4 mm) were diluted with glass beads (0.5—1 mm) to a constant volume. The void space of the reactor tube was filled with glass beads. Before the reaction, the catalysts were pre-treated in situ by feeding hydrogen (10 vol.% H_2 in N_2) for 1 h at 400 °C (Cu reduction). During all processes, nitrogen was used as carrier gas (50 cm^3 min^{-1}); ethanol was fed by a NE-300 syringe pump with WHSV 2.37 h^{-1} (7.7 mol% ethanol in N_2). Pentane was added as the internal standard (5 % molar concentration in ethanol feed). The tests were carried out at atmospheric pressure.

3 Result and discussion

3.1 Cu(II) phosphinate complex synthesis and structure

The reactions between the ligands $SAAP^{2-}$, $BSAAP^{2-}$, and $NAAP^{2-}$ (Figure 1) in the methanolic solution with the equimolar amount of the Cu^{2+} salt and sodium hydroxide lead to three new Cu(II) phosphinate complexes. Obtained compounds were isolated from the by-products by the dissolution of the dried reaction mixture in THF, filtration, drying, and crystallization of the pure products from acetonitrile solutions. Detailed synthetic procedures and the characterization of the ligands and complexes are described in Supporting Materials.

The single crystals were obtained for all three Cu(II) phosphinate complexes, and molecular structure models were obtained by single-crystal X-ray diffraction. Complex **1** crystallizes as a 1D polymer with the repeating formula unit {Cu(SAAP)}$_n$, while compounds **2** and **3** remain in the molecular form with the formulas [Cu$_6$(BSAAP)$_6$] and [Cu$_3$(NAAP)$_3$], respectively. The main crystallographic and refinement parameters are summarized in Table S1. For all three structures, the primary trend is that Cu^{2+} cations are coordinated in the ONO coordination pocket of the ligands (Figure 1).
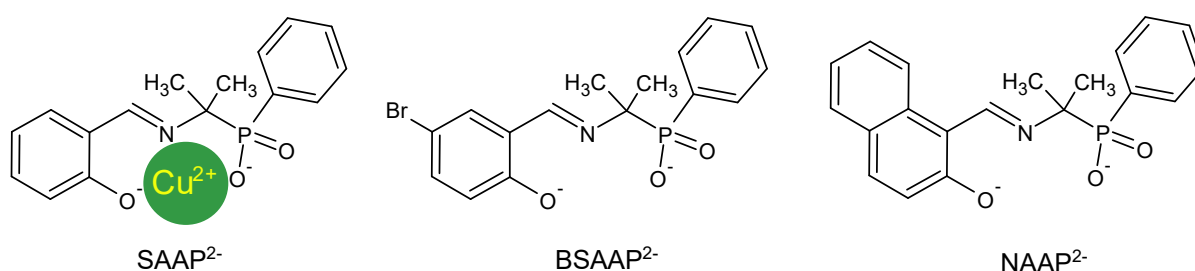

Figure 1. Schematic representation of the L^{2-} ligands used in this study. The green circle schematically depicts the copper(II) cation situated in the ONO coordination pocket of the $SAAP^{2-}$ ligand.

Further coordination and final arrangement of the Cu(II) phosphinate complexes are driven by the steric differences in the ligand molecules. The polymeric structure of **1** could be described as binuclear units Cu$_2$(SAAP)$_2$, consisting of two Cu(SAAP) moieties interconnected

5

to the cycle by the second phosphinic oxygen (not involved in the ONO coordination pocket) with a formation of two Cu—OPO—Cu bridges. The units are connected to the polymer chain by the mutual coordination of Cu^{2+} cations by phenolic oxygen atoms. All Cu^{2+} cations are five-coordinated by the ONO pocket atoms, one phosphinic, and one phenolic oxygen atom from two other ligands, as depicted in Figure 2 (coordination polyhedra will be discussed below).
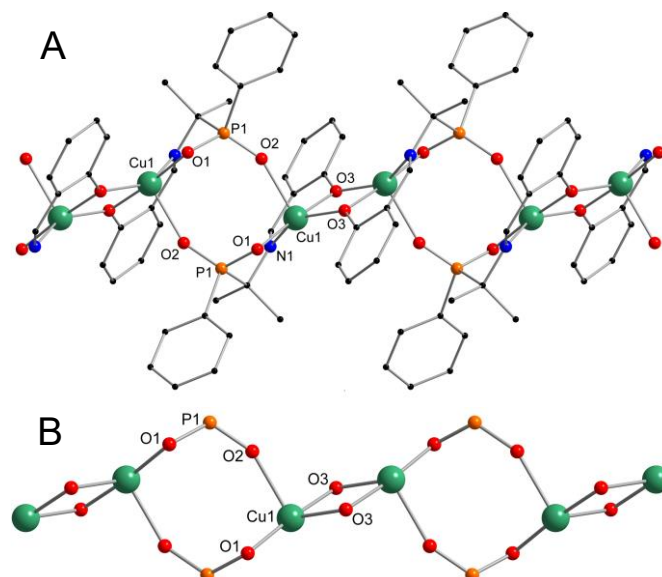

Figure 2. Ball and stick representation of the structure of **1**. The complete chain structure (A) and the phosphinate cores connected by the phenolic oxygen bridges (B). Color code: Cu green, P orange, O red, N blue, C black. Hydrogen atoms were omitted for the sake of clarity.

In the case of **2**, the formation of the centrosymmetric hexanuclear complex was observed. The whole molecular motive is more complicated than other complexes (Figure 3). Three independent Cu^{2+} centers of the molecule are four- (Cu1) and five-coordinated (Cu2 and Cu3). The Cu^{2+} coordination environments are based on an ONO coordination pocket and completed by a phosphinic oxygen atom of another ligand (Cu1) and one phosphinic and one phenolic oxygen atom from two other ligands (Cu2 and Cu3), as depicted in Figure 3.
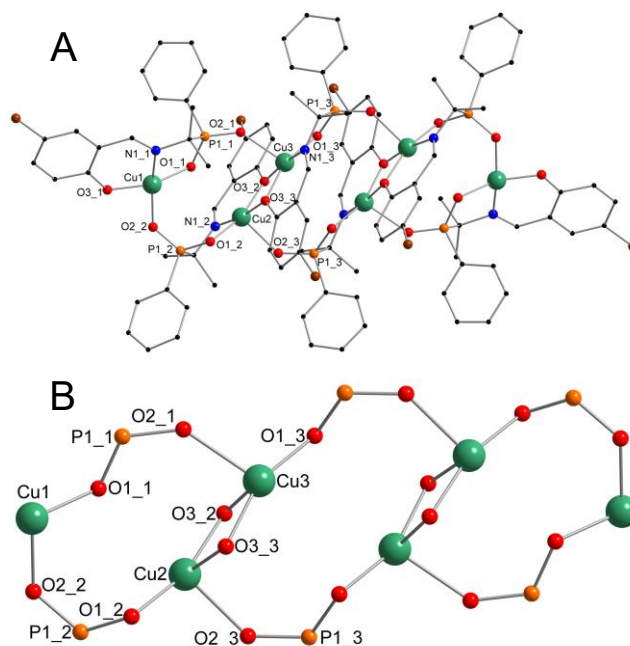
Figure 3. Ball and stick representation of the structure of **2**. The model of the molecule (A) and the core only (B). Color code: Cu green, P orange, O red, N blue, C black, Br brown. Hydrogen atoms were omitted for the sake of clarity.

The structure of the trinuclear molecular complex **3** is similar to the structure of **2**, if it was cut in half. In correspondence to **2,** Cu1 is four-coordinated, while Cu2 and Cu3 are five-coordinated. The main difference is that in **2** the Cu2 and Cu3 atoms are connected by two phenolic oxygen bridges, while in **3**, by one phenolic and one phosphinic oxygen bridge (Figure 4).
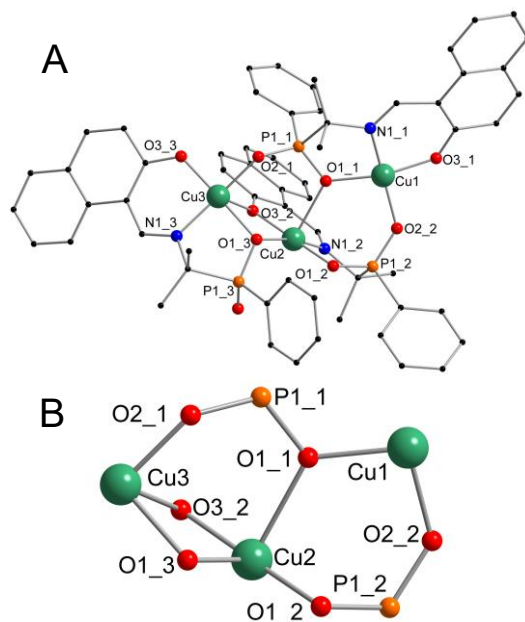
Figure 4. Ball and stick representation of the structure of **3**. The model of the molecule (A) and the core only (B). Color code: Cu green, P orange, O red, N blue, C black. Hydrogen atoms were omitted for the sake of clarity.

Selected bond lengths in the Cu polyhedra are summarized in Table S2 in Supplementary Materials. Continuous shape measures (CShM)[37–40] of the Cu^{2+} polyhedra for the formed complexes **1**—**3** showed that the geometry of five-coordinated polyhedra is closer to the square pyramidal in all cases than to trigonal bipyramidal with the distortion values in the range of 0.726—2.550 (see Table S3 in Supplementary Materials). The polyhedra of the four-coordinated Cu^{2+} cations in the complexes **2** and **3** are closer to square than tetrahedral geometry (see Table S3 in Supplementary Materials).

To confirm the molecular nature of the dissolved complexes **1**—**3** used in the catalyst preparation, their methanolic solutions were studied by ESI-MS spectroscopy. The spectra were recorded in positive and negative modes (Figure S1—S3). The coordination polymer **1** showed the presence of small molecular clusters with nuclearity from 2 to 5. The hexanuclear complex **2** featured the parent peak and also smaller fragments containing from 5 to 2 Cu atoms. In contrast, the trinuclear complex **3** displayed, beside the molecular parent peak, a dinuclear fragment, but also aggregated into larger species with 4 and 5 Cu atoms.

The behavior of Cu(II) phosphinate complexes **1**—**3** upon heating was analyzed by the TG/DSC method (Figures S4—S6). Complexes **1** and **3** showed thermal stability up to 250 ^{o}C, while complex **2** was stable practically to 300 °C. Above these temperatures, continuous weight losses were observed until 800 °C. The residual masses at 1000 ^{o}C were 40.21, 28.90, and 33.91 wt% for **1**—**3**, respectively. The values are in good correspondence with the calculated ones for the expected formation of $Cu_2P_2O_7$ from **1** (41.25 wt%), $Cu_3(PO_4)_2$ from **2** (28.59 wt%), and the $(Cu_2P_2O_7)_3(Cu_3(PO_4)_2)_2$ from **3** (33.43 wt%). Moreover, the absorption bands typical for phosphate group vibrations were observed in the IR spectra of Cu(II) phosphinate complexes after calcination at 500 °C for 10 h. Moreover, no absorption bands of the C–H stretches were observed in the 2800—3000 cm^{-1} region (Figure S7). Therefore, the temperature of 500 °C and 10 h calcination time were applied in the catalyst preparation (see Section 3.2).

3.2 Synthesis and characterization of Cu-phosphate/SiO₂ catalysts

Three Cu(II) phosphinate complexes **1**—**3** were used as precursors for copper deposition on porous commercial SiO_2 by wet impregnation to prepare **Cu-phosphate/SiO₂** catalysts (**CuP-1**—**3**). A benchmark sample was prepared by the dry impregnation method similar to a promising Cu/SiO_2 ethanol dehydrogenation catalyst working at 325 °C (**Cu-DI**).[20] Experimental loadings of Cu and P in the catalysts after calcination are summarized in Table 1. Cu contents in the **Cu-phosphate/SiO₂** catalysts were in the range from 1.75 to 2.33 wt%. The atomic Cu : P ratios were close to 1 : 1 in all three catalysts and thus followed the atomic Cu : P ratios in the starting Cu(II) phosphinate precursors.

Table 1. Experimental Cu and P loadings in the catalysts (ICP-OES).

Sample	Precursor	Cu loading [wt%]	P loading [wt%]	Cu : P mol ratio
CuP-1	{Cu(SAAP)}$_n$ (1)	1.79	0.93	0.93
CuP-2	[Cu$_6$(BSAAP)$_6$] (2)	2.33	1.13	1.0
CuP-3	[Cu$_3$(NAAP)$_3$] (3)	1.75	0.85	1.0
Cu-DI	Cu(NO$_3$)$_2$	2.42	-	-

All catalysts were prepared using the same silica support Aerosil 300 (284 m^2 g^{-1}, 1.55 cm^3 g^{-1}, isotherm shown in Figure S8). The porosity of **Cu-phosphate/SiO$_2$** samples was very similar to that of the catalyst support and the **Cu-DI** benchmark catalyst (Table 2). Surface areas (SA) ranged from 250 to 282 m^2 g^{-1}, pore volumes (V$_{total}$) from 1.04 to 1.14 cm^3 g^{-1}, and average pore diameters (d$_{pore}$) from 15 to 18 nm. The N$_2$ adsorption and desorption isotherms are shown in Figure S9 in Supplementary Materials.

Table 2. Comparison of the prepared catalysts by N$_2$ porosimetry.

Sample	SA [m^2 g^{-1}]	V$_{total}$ [cm^3 g^{-1}]	d$_{pore}$ [nm]^a
Aerosil 300	284	1.55	22
CuP-1	258	1.14	18
CuP-2	282	1.04	15
CuP- 3	250	1.10	18
Cu-DI	245	1.45	24

^{a}Estimated by $d_{pore} = \frac{4 \cdot V_{total}}{SA}$

Powder X-ray diffraction analysis showed that all **Cu-phosphate/SiO$_2$** catalysts prepared from the Cu(II) phosphinate complexes were X-ray amorphous after calcination in the ambient atmosphere (Figure 5). On the contrary, the sample prepared by dry impregnation of copper nitrate (**Cu-DI**) exhibited diffractions corresponding to copper(II) oxide (ICSD: 98-003-1059). According to the Debye-Scherrer equation, the crystallite size was estimated to be 22 nm.[20]
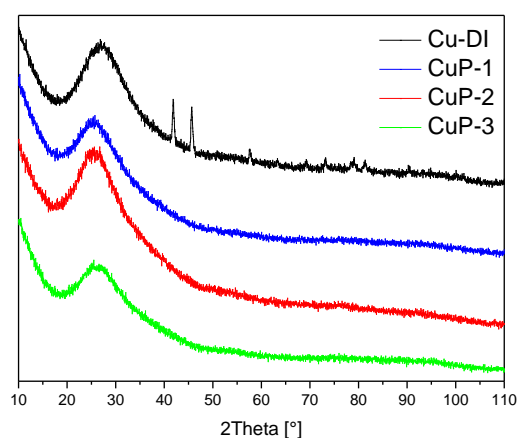
Figure 5. Comparison of the X-ray diffractograms of the fresh catalysts (calcined in the ambient atmosphere). **Cu-phosphate/SiO₂** samples are X-ray amorphous, and diffractions of CuO were observed (ICSD: 98-003-1059) for **Cu-DI**.

STEM-EDS analysis of the **Cu-phosphate/SiO₂** samples in all cases (**CuP-1—3**) displayed small and uniform particles (Figure 6). The sample **CuP-1** prepared from the polymer precursor {Cu(SAAP)}$_n$ showed the largest nanoparticles (Ā = 3.4 nm; σ = 0.9 nm) of the copper phosphate phase with a broader size distribution. Thus, the polymeric nature of the precursor (**1**) possibly leads to a slight increase in particle size in comparison with molecular ones ([Cu$_6$(BSAAP)$_6$] and [Cu$_3$(NAAP)$_3$]). It should be noted that the polymeric complex (**1**) can dissociate in solution into fragments with varying nuclearity (ESI-MS, see discussion above), potentially resulting in a broader size distribution of the resulting nanoparticles. Based on the graphic analysis of the STEM micrograph survey, particles in **CuP-2** prepared from [Cu$_6$(BSAAP)$_6$] exhibited the NPs size of Ā = 2.1 nm and σ = 0.5 nm. On the other hand, the **CuP-3** catalyst prepared from [Cu$_3$(NAAP)$_3$] showed slightly larger particles (Ā = 2.7 nm; σ = 0.5 nm), despite the molecules of **3** (precursor for **CuP-3**) being smaller than **2**. According to STEM-EDS elemental mapping, these particles consist of Cu and P (Figure 7). Thus, it can be inferred that the particles observed in STEM-EDS micrographs present an amorphous copper phosphate phase (see below for XRD, TG/DSC, IR, and XPS spectroscopy study).
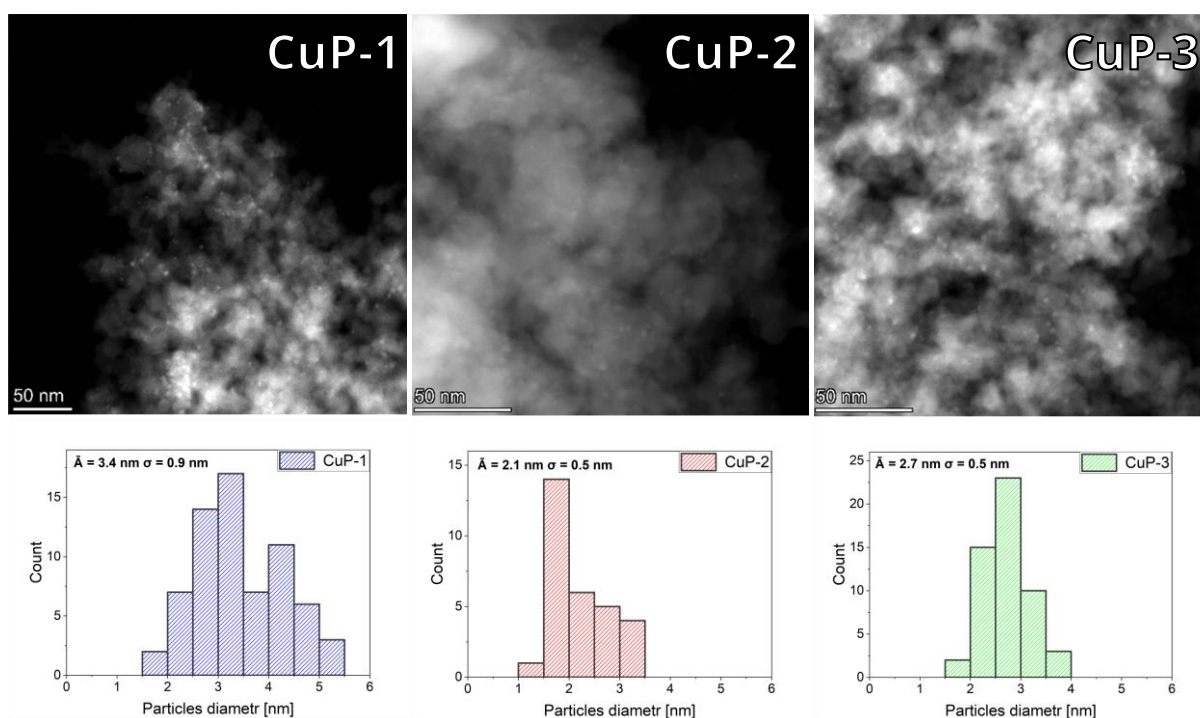

Figure 6. STEM micrographs of samples **CuP-1—3** after calcination (up) and comparison of their particle size distribution histograms (below).
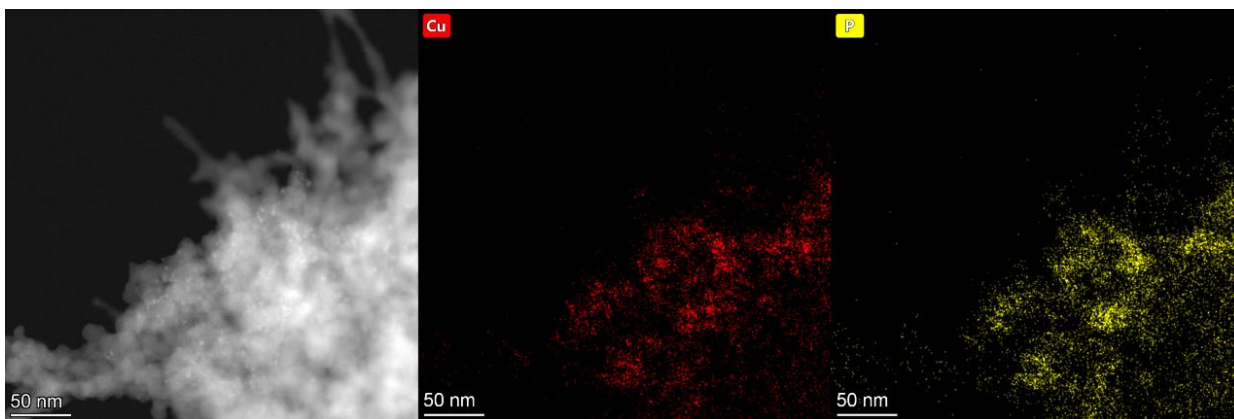
Figure 7. STEM micrograph of **CuP-1** after calcination and STEM-EDS elemental micrograph survey of copper (red) and phosphorus (yellow).

3.3 Catalysis

Ethanol conversion over **CuP-1—3**, and **Cu-DI** catalysts at 325 °C is shown in Figure 8. A remarkable difference in catalysts performance with time was observed between the **Cu-phosphate/SiO₂** catalysts and phosphorus-free **Cu-DI** (Figures 8 and 9). The sample prepared by the dry impregnation method (**Cu-DI**) achieved ethanol conversion up to 95 % at the beginning of the catalytic process. The sample showed rapid deactivation during the first 5 h of the measurement (ethanol conversion dropped to ca. 70 %). Afterwards, the deactivation was much slower until the end of the catalytic experiment, with ethanol conversion being ca. 60 % after 50 h. This behavior is in good agreement with numerous studies that have pointed out that the copper-based catalysts supported on silica often suffer from deactivation.[7,16–18,41,42]

In contrast, the samples prepared from Cu(II) phosphinate complexes showed an initial increase in catalytic activity during the first 1.6—8 h before reaching the maximum ethanol conversion (3.3—10 h). The maximum ethanol conversion reached ca. 75 % for **CuP-1**, ca. 40 % for **CuP-2**, and ca. 60 % for **CuP-3**, as shown in Figure 8. After 6—13 h of the catalytic experiment, the course of this reaction changed, and the catalysts gradually began to deactivate. Additional catalytic experiments and analyses (ICP-OES, XPS, and STEM-EDS) were performed to understand better the catalytic behavior of the **Cu-phosphate/SiO₂** catalysts. These results are thoroughly discussed in Section 3.4.

The catalytic activity of the **Cu-phosphate/SiO₂** samples seemingly displayed a size dependence. Surprisingly, the most active catalyst was **CuP-1** possessing the largest particles (Ā = 3.4 nm; σ = 0.9 nm), while the least active was **CuP-2** with the smallest particles (Ā = 2.1 nm; σ = 0.5 nm). The surface areas of the **Cu-phosphate/SiO₂** samples were similar, in the range of 250—282 m^2 g^{-1}, and probably did not significantly affect catalytic activity. Also, sample **CuP-2** exhibited the highest copper loading (2.33 wt%), but it displayed the lowest catalytic activity compared to **CuP-1** and **CuP-3,** with copper loading of 1.79 wt% and 1.75 wt%, respectively. Notably, the particle size was controlled by the Cu phosphinate complex used in the catalyst preparation and thus, the precursor choice influenced the catalytic

activity of the final material. The trend in catalytic activity seems to disagree with the reports describing ethanol dehydrogenation over Cu NPs, where the smaller particles usually provide higher catalytic performance.[43] However, a thorough characterization is needed to understand better the catalytic properties of **Cu-phosphate/SiO₂** materials (see Section 3.4).

Both **Cu-phosphate/SiO₂** and phosphate-free **Cu-DI** catalysts exhibited very high selectivity to acetaldehyde (≥ 95 % for **Cu-DI** and ≥ 98 % for **Cu-phosphate/SiO₂**) with a carbon balance fluctuating around 95 %. Therefore, the acetaldehyde yields closely followed the ethanol conversion (Figures 8 and 9).
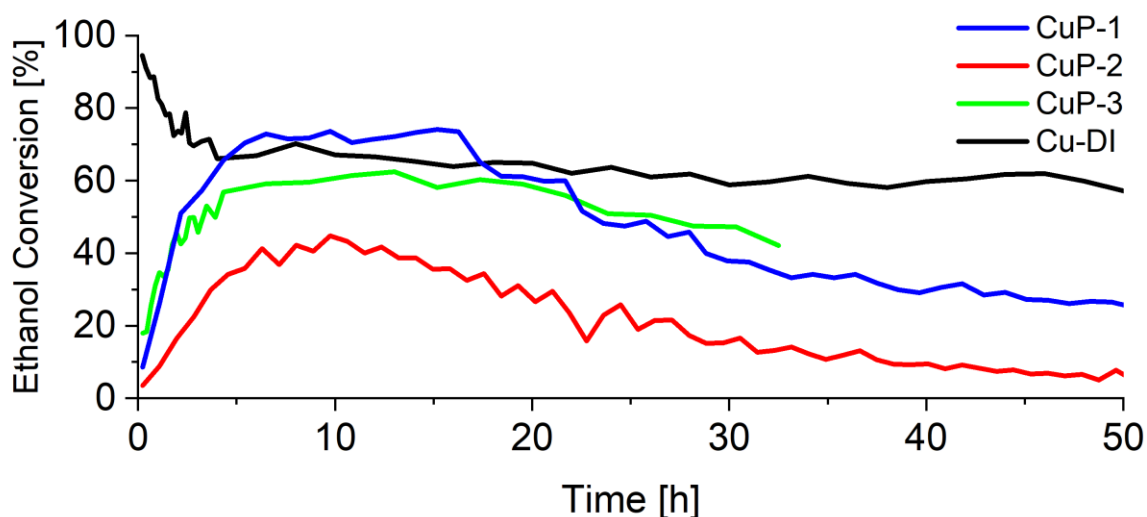

Figure 8. Comparison of the catalysts prepared from different precursors and their effect on ethanol conversion.
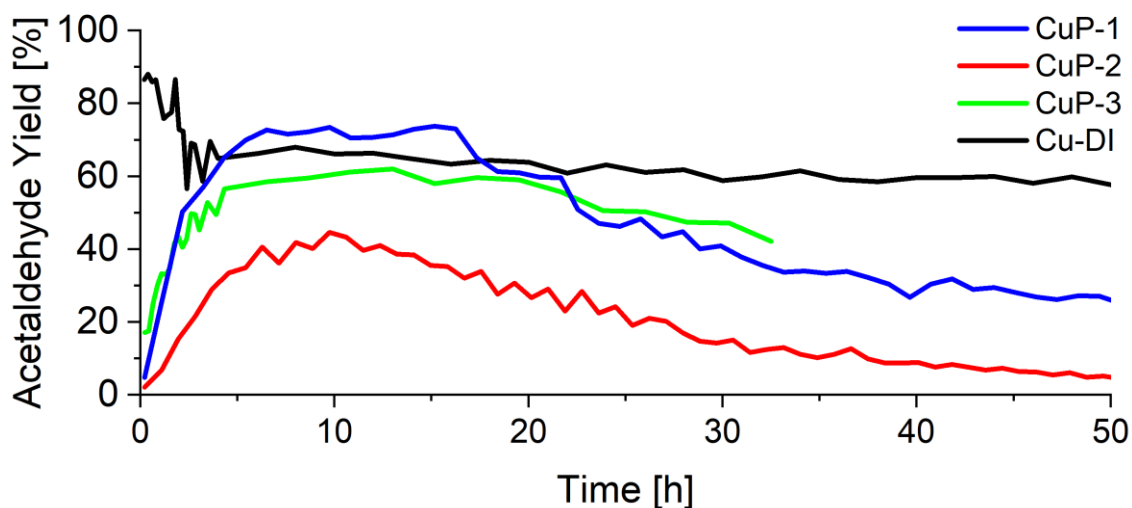

Figure 9. Acetaldehyde yield over the **Cu-phosphate/SiO₂** catalysts and comparison with the **Cu-DI** benchmark sample.

Table 3 presents a comparison of previously reported catalysts and the most active newly developed **Cu-phosphate/SiO₂** catalyst **CuP-1** from this study presented at its maximum

catalytic activity. **CuP-1** shows a promising activity compared to other Cu-based catalysts. Despite the relatively low Cu loading of 1.79 wt%, **CuP-1** can achieve high acetaldehyde productivity with high selectivity. However, its stability needs further improvement.

Table 3. Comparison of acetaldehyde productivity at 325 °C of **Cu-phosphate/SiO$_2$** catalyst **CuP-1** (at the maximum activity) with the data presented in literature.

Sample	Cu [wt%]	WHSV [h^{-1}]	T [°C]	Conversion [%]	Acetaldehyde selectivity [%]	Acetaldehyde productivity [g g^{-1} h^{-1}]
CuP-1[This work]	1.79	2.37	325	73	≥ 98	1.70
Cu/SiO$_2$[42]	25	2.37	300	75	94	1.67
Cu/SiO$_2$-AE[16]	2.7	3.16	300	98	≥99	3.07
Cu/SiO$_2$[20]	2.42	4.73	325	50	95	2.24
Cu/β Zeolite[17]	5	1	325	91	79	0.72

3.4 Changes to the Cu-phosphate/SiO$_2$ catalysts during time-on-stream

Additional analyses were performed to understand the peculiar catalytic performance of the **Cu-phosphate/SiO$_2$** samples. The Cu : P ratio was ex-situ analyzed by ICP-OES analysis for **CuP-1** at different stages of the catalyst life: (i) calcined in ambient atmosphere, (ii) after H$_2$ treatment, (iii) at the maximum of ethanol conversion (i.e., after 7 h of TOS), and (iv) at the end of the catalytic experiment (after more than 50 h of TOS; Table 4). It can be seen that the Cu : P ratio did not change after H$_2$ treatment in comparison to the fresh calcined sample; in both cases the ratio stayed close to 1 according to ICP-OES. During the ethanol dehydrogenation process the amount of phosphorus steadily declined; the Cu : P ratio increased to 1.15 for the sample at the top of catalytic activity and to 1.72 at the end of catalytic test (Table 4).

Table 4. ICP-OES analysis of **CuP-1** at the different stages of catalyst life.

Sample	Cu : P mol ratio
Calcined	0.94
H$_2$ treated	0.93
At the top of catalytic activity	1.2
Spent catalyst	1.7

Nanoparticle sizes at the different stages of **CuP-1** catalyst lifetime were monitored by ex-situ STEM analyses (Figure 10). Particles in the sample after H$_2$ treatment (Ā = 3.4 nm; σ = 0.9) were similar compared to the fresh catalyst, agreeing with no dramatic changes (Figure 10A and B). The increase of the catalyst activity was followed by a significant nanoparticles size decrease (Ā = 2.4 nm; σ = 0.5 nm) (**CuP-1** at the maximum catalytic activity; Figure 10C). STEM

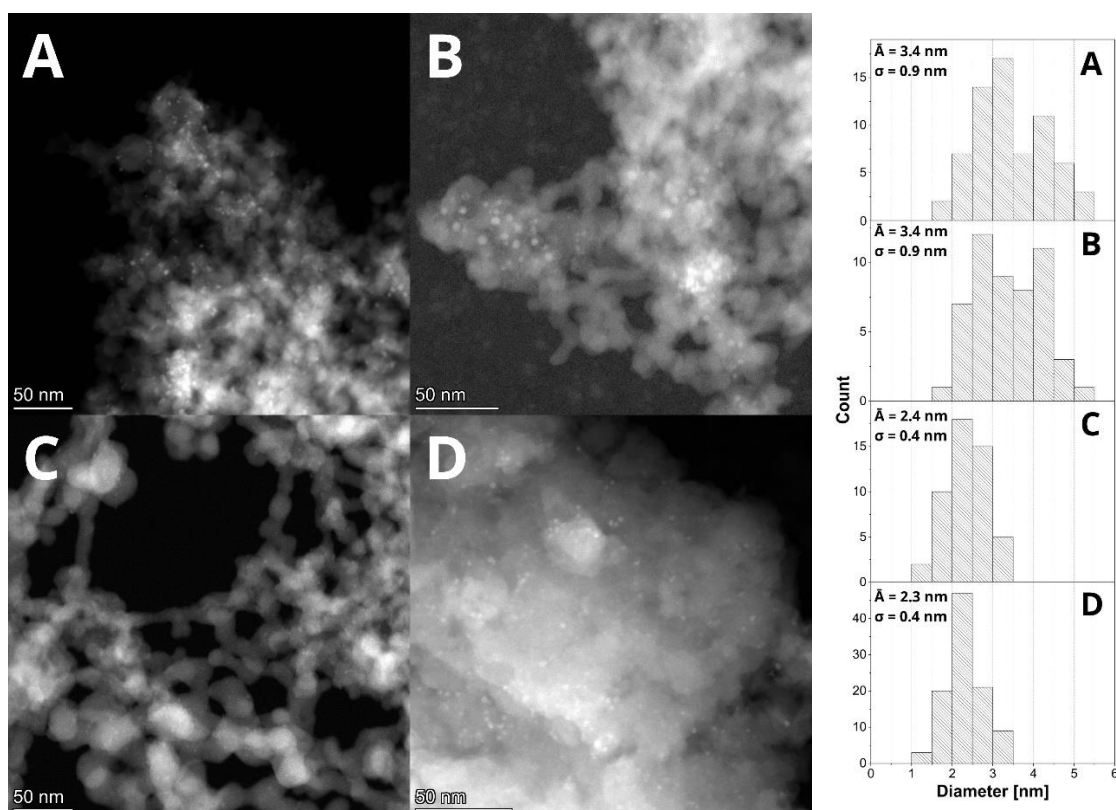characterization of the spent catalyst (Figure 10D) revealed a continuous decrease in the nanoparticle size.

Figure 10. STEM micrographs of catalyst **CuP-1** after calcination (A), after H_2 treatment (B), at the point of the highest catalytic activity (C), and after the whole catalytic cycle (D).

The **Cu-phosphate/SiO₂** catalysts remained X-ray amorphous after the whole catalytic cycle (Figure 11). In contrast, the **Cu-DI** sample was reduced to metallic copper (ICSD: 98-062-7113) after the catalytic reaction. Moreover, as we reported recently, **Cu-DI** was reduced to metallic copper already after the H_2 treatment. Crystallite sizes estimated by the Debye-Scherrer equation for **Cu-DI** after both H_2 treatment and the whole catalytic cycle remained similar (ca. 22 nm).[20]
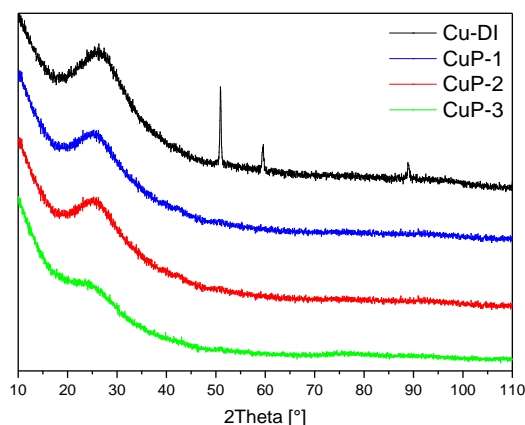
Figure 11. XRD diffraction pattern of spent catalysts, **Cu-phosphate/SiO₂** samples remained amorphous, diffractions of metallic copper were observed (ICSD: 98-062-7113) for **Cu-DI**.

XPS spectra were recorded at different stages of the **CuP-1** catalyst lifetime. Both fresh calcined and H_2-treated catalysts unambiguously contain Cu^{2+} species represented by a peak at 934.3 eV[44] and a satellite peak at ~944 eV typical for Cu^{2+} species[45] (Figure 12 A and B). No evident changes were observed during the hydrogen treatment step (1 h, 400 °C). The reduction of Cu^{2+} species was observed at the maximum catalytic activity (Figure 12 C). Cu^{2+} species were reduced entirely in the spent catalyst to Cu^0/Cu^+ (peak at 932.8 eV). Unfortunately, Cu^0 and Cu^+ cannot be distinguished using Cu 2p peak[46] (Figure 12 D), and the surface copper concentration is too low to observe Cu LMM signal (Auger electrons).[20] The surface elemental composition for the different stages of catalyst lifetime, derived from XPS analyses, is presented in Table 5. The copper mass fraction increased according to XPS in the sample at the maximum of catalytic activity (0.83 wt%), then decreased for the spent catalyst (0.24 wt%). The amount of phosphorus in the surface of the spent catalyst significantly declined (Table 5).
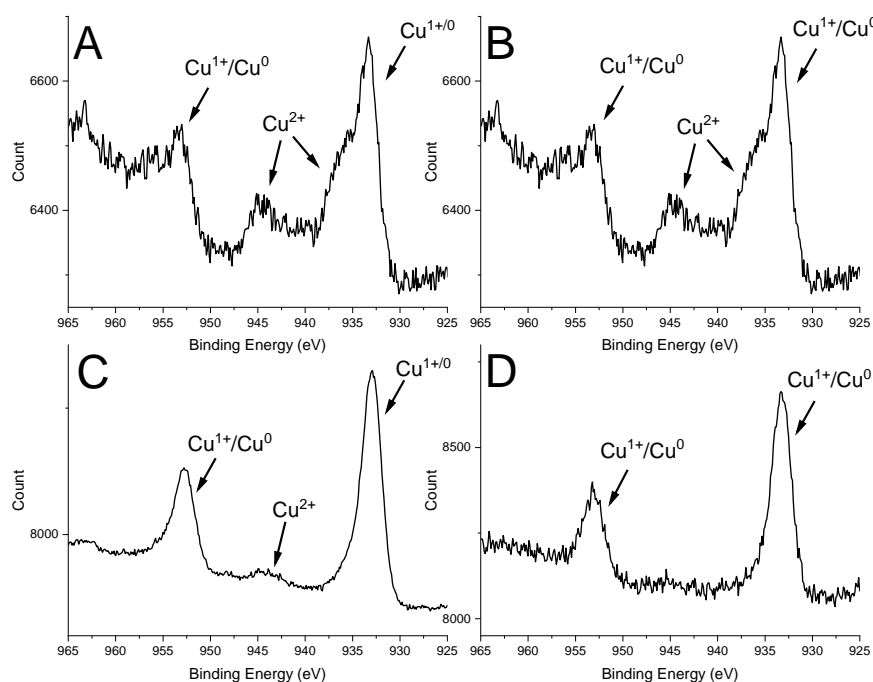
Figure 12. High-resolution XPS spectra (Cu 2p) recorded for catalyst **CuP-1** after calcination (A), after H_2 treatment (B), at the point of the highest catalytic activity (C), and after the whole catalytic cycle (D).

Table 5. XPS analysis of **CuP-1** at the different stages of catalyst lifetime.

Sample	Cu conc. [wt%]	P conc. [wt%]	Cu conc. [mol%]	P conc. [mol%]	Cu : P mol ratio
Calcined	0.21	0.34	0.07	0.23	0.30
H_2 treated	0.31	0.45	0.10	0.30	0.33
Top activity	0.83	0.50	0.27	0.33	0.83
Spent catalyst	0.24	0.05	0.07	0.03	2.3

Based on the results of XRD, ICP-OES, STEM-EDS, and XPS analyses described above, we propose a hypothesis regarding the possible activation and deactivation mechanisms in the **Cu-phosphate/SiO₂** catalysts. First, Cu^{2+} species in the **Cu-phosphate/SiO₂** catalysts were not reduced (XPS) after H_2 treatment and therefore were inactive. Cu reduction before ethanol dehydrogenation is a common pretreatment step and leads to catalyst activation.[16,47] Moreover, in contrast to the **Cu-phosphate/SiO₂** catalysts, the XRD analysis of the spent **Cu-DI** catalyst showed the presence of metallic copper (Figure 11). A possible explanation for the ineffective H_2 treatment of the **Cu-phosphate/SiO₂** catalysts could be the presence of the Cu-phosphate phase with an intimate Cu and P mixing, as suggested by STEM-EDS analyses (see

Section 3.2). Metal phosphates are generally much more resistant to reduction than corresponding metal oxides.[48]

The activated **CuP-1** catalyst exhibited a higher Cu : P ratio both in bulk and the surface layer (ICP-OES, Table 1; XPS, Table 5), smaller particle size (STEM; Figure 10), and a higher Cu surface content (XPS; Table 5) than the non-active (freshly calcined) sample. Also, the Cu^{2+} species mainly were reduced to Cu^0/Cu^{1+} during the time-on-stream (TOS) according to XPS analyses (Figure 12). Apparently, the phosphorus leaching from the **Cu-phosphate/SiO₂** catalysts during TOS enabled Cu reduction. These processes could be simultaneous. Ethanol and H_2 (originating in ethanol dehydrogenation) can be put forward as possible reducing agents. As already discussed, Cu reduction is necessary for its activation in ethanol dehydrogenation reaction. The decrease in particle size and increase in the Cu surface content may also have a beneficial effect on catalytic activity as well. It correlates well with the observed increase in catalytic activity during the first 1.6—8.3 h of catalytic reaction in **CuP-1—3**.

Finally, the **Cu-phosphate/SiO₂** samples started to deactivate after a period of high catalytic activity. Two deactivation mechanisms are primarily discussed in the literature: sintering of Cu particles and coking.[16–18,41] Cu sintering has not been observed in our case: the samples stayed XRD amorphous (Figure 11), and no large particles were observed by STEM-EDS (Figure 10). Therefore, we focused our attention on possible coking and analyzed the carbon content by XPS. The XPS analysis of the catalyst surface suggests that there is no significant coking, as the carbon content at the maximum of catalytic activity (3.49 wt%) is virtually the same as in that of the spent catalyst after 50 h of TOS (3.51 wt%), as shown in Table 6. The presence of coking is usually clearly observed after such extensive TOS.[20] Notably, our findings agree with previous studies, which suggest that adding phosphorus to zeolite catalysts can prevent coking.[29,30] Based on the results, an alternative deactivation mechanism can be suggested. The STEM-EDS micrographs of spent catalyst demonstrate a significant decrease in particle size (from 3.4 to 2.3 nm on average; ~32 %). At the same time, the Cu surface content significantly decreased (XPS; Table 5). Therefore, we hypothesize that Cu diffuses into the SiO_2 support, becomes inaccessible, and in turn, inactive. The Cu diffusion in silica-based catalysts has already been observed at the temperatures below T_{Tamman}.[21]

Table 6. The study of coking by XPS analysis of **CuP-1** at the different stages of catalyst life.

Sample	Carbon content [wt%]
Calcined	2.24
H₂ treated	3.74
Top activity	3.49
Spent catalyst	3.51

Conclusions

In this study, three new Cu-phosphate-based catalysts were prepared using three newly synthesized well-soluble Cu(II) phosphinate complexes of different nuclearity: a polymeric (**1**),

a hexanuclear (**2**), and a trinuclear (**3**) complex. The structures of complexes **1**—**3** were fully characterized and described in detail. Impregnation of the molecular precursors **1**—**3** on silica provided **Cu-phosphate/SiO₂** materials with homogeneously dispersed nanoparticles (2.1—3.4 nm) and narrow particle size distribution. The polymeric complex (**1**) provided larger particles with broader distribution than the hexanuclar (**2**) and trinuclear (**3**) complexes. The particles consisted of both Cu and P according to STEM-EDS analyses. The **Cu-phosphate/SiO₂** materials were evaluated as catalysts in non-oxidative ethanol dehydrogenation and compared with the conventional benchmark Cu-based catalyst prepared by dry impregnation (**Cu-DI**). Our results demonstrate a distinctively different catalytic behavior of the **Cu-phosphate/SiO₂** materials compared to the conventional Cu-based catalysts. By investigating the catalyst (**CuP-1**) life cycle, we uncovered the changes to the material influencing the catalytic properties. The increase of catalytic activity during TOS was related to the decrease of phosphorus content in both bulk and the surface layer and to the copper reduction. The maximum ethanol conversion was reached during 1.6—8 h of TOS, namely: ca. 75 % for **CuP-1**, ca. 40 % for **CuP-2**, and ca. 60 % for **CuP-3**, while selectivity to acetaldehyde remained over 98 % at WHSV = 2.37 h^{-1} for all catalysts. However, a steady decrease in catalytic activity was observed after the catalysts reached their maximum performance. Contrary to earlier reported Cu-based catalysts, **Cu-phosphate/SiO₂** exhibited no coking. The deactivation process was suggested to be related to the Cu diffusion: the surface Cu concentration decreased together with the average particle size. Overall, our study demonstrates a new approach to P-doped Cu-based catalysts with intimate Cu and P mixing and sheds light on their peculiar behavior in non-oxidative ethanol dehydrogenation.

ACKNOWLEDGMENTS

References

(1)   Graedel, T. Green Chemistry in an Industrial Ecology Context. *Green Chem.* **1999**, *1* (5), 126–128. DOI:10.1039/a908574b.

(2)   Clark, J. H. Green Chemistry: Challenges and Opportunities. *Green Chem.* **1999**, *1* (1), 1–8. DOI:10.1039/a807961g.

(3)   Liu, P.; Hensen, E. J. M. Highly Efficient and Robust Au/MgCuCr2O4 Catalyst for Gas-Phase Oxidation of Ethanol to Acetaldehyde. *J. Am. Chem. Soc.* **2013**, *135* (38), 14032–14035. DOI:10.1021/ja406820f.

(4)   Takei, T.; Iguchi, N.; Haruta, M. Synthesis of Acetoaldehyde, Acetic Acid, and Others

by the Dehydrogenation and Oxidation of Ethanol. *Catal. Surv. from Asia* **2011**, *15* (2), 80–88. DOI:10.1007/s10563-011-9112-1.

(5)   Patel, A. C.; Li, S.; Wang, C.; Zhang, W.; Wei, Y. Electrospinning of Porous Silica Nanofibers Containing Silver Nanoparticles for Catalytic Applications. *Chem. Mater.* **2007**, *19* (6), 1231–1238. DOI:10.1021/cm061331z.

(6)   Cespi, D.; Passarini, F.; Vassura, I.; Cavani, F. Butadiene from Biomass, a Life Cycle Perspective to Address Sustainability in the Chemical Industry. **2016**, 1625–1638. DOI:10.1039/c5gc02148k.

(7)   Pomalaza, G.; Arango Ponton, P.; Capron, M.; Dumeignil, F. Ethanol-to-Butadiene: The Reaction and Its Catalysts. *Catal. Sci. Technol.* **2020**, *10* (15), 4860–4911. DOI:10.1039/d0cy00784f.

(8)   Shylesh, S.; Gokhale, A. A.; Scown, C. D. From Sugars to Wheels : The Conversion of Ethanol to Catalysts. **2016**, 1462–1472. DOI:10.1002/cssc.201600195.

(9)   Jira, R. Acetaldehyde from Ethylene - A Retrospective on the Discovery of the Wacker Process. *Angew. Chemie - Int. Ed.* **2009**, *48* (48), 9034–9037. DOI:10.1002/anie.200903992.

(10) Keith, J. A.; Nielsen, R. J.; Oxgaard, J.; Goddard, W. A. Unraveling the Wacker Oxidation Mechanisms. *J. Am. Chem. Soc.* **2007**, *129* (41), 12342–12343. DOI:10.1021/ja072400t.

(11) Lebedev Process. In *Comprehensive Organic Name Reactions and Reagents*; John Wiley & Sons, Inc.: Hoboken, NJ, USA, 2010. DOI:10.1002/9780470638859.conrr387.

(12) Angelici, C.; Velthoen, M. E. Z.; Weckhuysen, B. M.; Bruijnincx, P. C. A. Influence of Acid–Base Properties on the Lebedev Ethanol-to-Butadiene Process Catalyzed by SiO2–MgO Materials. *Catal. Sci. Technol.* **2015**, *5* (5), 2869–2879. DOI:10.1039/C5CY00200A.

(13) Segawa, A.; Nakashima, A.; Nojima, R.; Yoshida, N.; Okamoto, M. Acetaldehyde Production from Ethanol by Eco-Friendly Non-Chromium Catalysts Consisting of Copper and Calcium Silicate. *Ind. Eng. Chem. Res.* **2018**, *57* (35), 11852–11857. DOI:10.1021/acs.iecr.8b02498.

(14) Freitas, I. C.; Damyanova, S.; Oliveira, D. C.; Marques, C. M. P.; Bueno, J. M. C. Effect of Cu Content on the Surface and Catalytic Properties of Cu/ZrO2 Catalyst for Ethanol Dehydrogenation. *J. Mol. Catal. A Chem.* **2014**, *381*, 26–37. DOI:10.1016/j.molcata.2013.09.038.

(15) Chang, F. W.; Yang, H. C.; Roselin, L. S.; Kuo, W. Y. Ethanol Dehydrogenation over Copper Catalysts on Rice Husk Ash Prepared by Ion Exchange. *Appl. Catal. A Gen.* **2006**, *304* (1–2), 30–39. DOI:10.1016/j.apcata.2006.02.017.

(16) Zhang, H.; Tan, H. R.; Jaenicke, S.; Chuah, G. K. Highly Efficient and Robust Cu Catalyst for Non-Oxidative Dehydrogenation of Ethanol to Acetaldehyde and Hydrogen. *J. Catal.* **2020**, *389*, 19–28. DOI:10.1016/J.JCAT.2020.05.018.

(17) Yu, D.; Dai, W.; Wu, G.; Guan, N.; Li, L. Stabilizing Copper Species Using Zeolite for Ethanol Catalytic Dehydrogenation to Acetaldehyde. *Chinese J. Catal.* **2019**, *40* (9), 1375–1384. DOI:10.1016/S1872-2067(19)63378-4.

(18) Ob-Eye, J.; Praserthdam, P.; Jongsomjit, B. Dehydrogenation of Ethanol to Acetaldehyde over Different Metals Supported on Carbon Catalysts. *Catalysts* **2019**, *9* (1). DOI:10.3390/catal9010066.

(19) Chang, F. W.; Kuo, W. Y.; Lee, K. C. Dehydrogenation of Ethanol over Copper Catalysts on Rice Husk Ash Prepared by Incipient Wetness Impregnation. *Appl. Catal. A Gen.* **2003**, *246* (2), 253–264. DOI:10.1016/S0926-860X(03)00050-4.

(20) Pokorny, T.; Vykoukal, V.; Machac, P.; Moravec, Z.; Scotti, N.; Roupcova, P.; Styskalik, A. Ethanol Dehydrogenation over Copper-Silica Catalysts: From Atomic Distribution to 15nm Large Particles. **2022**. DOI:10.26434/CHEMRXIV-2022-RJB5H.

(21) Pampararo, G.; Garbarino, G.; Riani, P.; Vykoukal, V.; Busca, G.; Debecker, D. P. Ethanol Dehydrogenation to Acetaldehyde with Mesoporous Cu-SiO2 Catalysts Prepared by Aerosol-Assisted Sol–Gel. *Chem. Eng. J.* **2023**, *465* (January), 142715. DOI:10.1016/j.cej.2023.142715.

(22) Tu, Y. J.; Chen, Y. W. Effects of Alkali Metal Oxide Additives on Cu/SiO2 Catalyst in the Dehydrogenation of Ethanol. *Ind. Eng. Chem. Res.* **2001**, *40* (25), 5889–5893. DOI:10.1021/ie010272q.

(23) Coles, M. P.; Lugmair, C. G.; Terry, K. W.; Tilley, T. D. Titania-Silica Materials from the Molecular Precursor Ti[OSi(O(t)Bu)3]4: Selective Epoxidation Catalysts. *Chem. Mater.* **2000**, *12* (1), 122–131. DOI:10.1021/CM990444Y/ASSET/IMAGES/LARGE/CM990444YF00007.JPEG.

(24) Jarupatrakorn, J.; Tilley, T. D. Silica-Supported, Single-Site Titanium Catalysts for Olefin Epoxidation. A Molecular Precursor Strategy for Control of Catalyst Structure. *J. Am. Chem. Soc.* **2002**, *124* (28), 8380–8388. DOI:10.1021/JA0202208/ASSET/IMAGES/LARGE/JA0202208F00008.JPEG.

(25) Singh, A.; Chang, S. L. Y.; Hocking, R. K.; Bach, U.; Spiccia, L. Highly Active Nickel Oxide Water Oxidation Catalysts Deposited from Molecular Complexes. *Energy Environ. Sci.* **2013**, *6* (2), 579–586. DOI:10.1039/C2EE23862D.

(26) Yamamoto, T.; Shimoda, A.; Okuhara, T.; Misono, M. A Promoting Effect of Phosphorus-Addition to Cu/SiO2 on Selective Synthesis of Formaldehyde by Dehydrogenation of Methanol. *Chem. Lett.* **1988**, *17* (2), 273–276. DOI:10.1246/cl.1988.273.

(27) Qi, X.; Zhang, L.; Xie, W.; Ji, T.; Li, R. Synthesis of Copper-Substituted Aluminophosphate Molecular Sieves (CuAPO-11) and Their Catalytic Behavior for Phenol Hydroxylation. *Appl. Catal. A Gen.* **2004**, *276* (1–2), 89–94. DOI:10.1016/J.APCATA.2004.07.043.

(28) Siva Kumar, V.; Padmasri, A. H.; Satyanarayana, C. V. V.; Ajit Kumar Reddy, I.; David Raju, B.; Rama Rao, K. S. Nature and Mode of Addition of Phosphate Precursor in the

Synthesis of Aluminum Phosphate and Its Influence on Methanol Dehydration to Dimethyl Ether. *Catal. Commun.* **2006**, *7* (10), 745–751. DOI:10.1016/j.catcom.2006.02.025.

(29)   van der Bij, H. E.; Weckhuysen, B. M. Phosphorus Promotion and Poisoning in Zeolite-Based Materials: Synthesis, Characterisation and Catalysis. *Chem. Soc. Rev.* **2015**, *44* (20), 7406–7428. DOI:10.1039/C5CS00109A.

(30)   Xia, W.; Huang, Y.; Ma, C.; Li, S.; Wang, X.; Chen, K.; Liu, D. Multiple Important Roles of Phosphorus Modification on the ZSM-5 in Ethanol to Olefin Reaction: Acidity Adjustment, Hydrothermal Stability and Anti-Coking. *Fuel* **2023**, *341* (January), 127675. DOI:10.1016/j.fuel.2023.127675.

(31)   Schneider, C. A.; Rasband, W. S.; Eliceiri, K. W. NIH Image to ImageJ: 25 Years of Image Analysis. *Nat. Methods* **2012**, *9* (7), 671–675. DOI:10.1038/nmeth.2089.

(32)   Hooft, R. W. W. Collect: Data Collection Software. Nonius BV: Delft 1998.

(33)   Otwinowski, Z.; Minor, W. Processing of X-Ray Diffraction Data Collected in Oscillation Mode. *Methods Enzymol.* **1997**, *276* (January 1993), 307–326. DOI:10.1016/S0076-6879(97)76066-X.

(34)   Sheldrick, G. M. SADABS-Bruker Nonius Scaling and Absorption Correction. Bruker AXS Inc.: Madison, Wisconsin, USA 2003.

(35)   Sheldrick, G. M. SHELXT – Integrated Space-Group and Crystal-Structure Determination. *Acta Crystallogr. Sect. A Found. Adv.* **2015**, *71* (1), 3–8. DOI:10.1107/S2053273314026370.

(36)   Sheldrick, G. M. Crystal Structure Refinement with SHELXL. *Acta Crystallogr. Sect. C Struct. Chem.* **2015**, *71* (1), 3–8. DOI:10.1107/S2053229614024218.

(37)   Llunell, M.; Casanova, D.; Cirera, J.; Alemany, P.; Alvarez, S. Users Manual: SHAPE. Program for the Stereochemical Analysis of Molecular Fragments by Means of Continuous Shape Measures and Associated Tools. 2013, pp 1–35.

(38)   Pinsky, M.; Avnir, D. Continuous Symmetry Measures. 5. The Classical Polyhedra. *Inorg. Chem.* **1998**, *37* (21), 5575–5582. DOI:10.1021/ic9804925.

(39)   Cirera, J.; Alemany, P.; Alvarez, S. Mapping the Stereochemistry and Symmetry of Tetracoordinate Transition-Metal Complexes. *Chem. Eur. J.* **2004**, *10* (1), 190–207. DOI:10.1002/chem.200305074.

(40)   Alvarez, S.; Llunell, M. Continuous Symmetry Measures of Penta-Coordinate Molecules: Berry and Non-Berry Distortions of the Trigonal Bipyramid. *J. Chem. Soc. Dalt. Trans.* **2000**, No. 19, 3288–3303. DOI:10.1039/b004878j.

(41)   Campisano, I. S. P.; Rodella, C. B.; Sousa, Z. S. B.; Henriques, C. A.; Teixeira da Silva, V. Influence of Thermal Treatment Conditions on the Characteristics of Cu-Based Metal Oxides Derived from Hydrotalcite-like Compounds and Their Performance in Bio-Ethanol Dehydrogenation to Acetaldehyde. *Catal. Today* **2018**, *306*, 111–120. DOI:10.1016/j.cattod.2017.03.017.

(42) Amokrane, S.; Boualouache, A.; Simon, P.; Capron, M.; Otmanine, G.; Allam, D.; Hocine, S. Effect of Adding Transition Metals to Copper on the Dehydrogenation Reaction of Ethanol. *Catal. Letters* **2021**, *151* (10), 2864–2883. DOI:10.1007/s10562-020-03517-0.

(43) Zhang, H.; Tan, H.-R.; Jaenicke, S.; Chuah, G.-K. Highly Efficient and Robust Cu Catalyst for Non-Oxidative Dehydrogenation of Ethanol to Acetaldehyde and Hydrogen. *J. Catal.* **2020**, *389*, 19–28. DOI:10.1016/j.jcat.2020.05.018.

(44) Yu, J.; Yang, M.; Zhang, J.; Ge, Q.; Zimina, A.; Pruessmann, T.; Zheng, L.; Grunwaldt, J.; Sun, J. Stabilizing Cu + in Cu/SiO 2 Catalysts with a Shattuckite-Like Structure Boosts CO 2 Hydrogenation into Methanol. *ACS Catal.* **2020**, *10* (24), 14694–14706. DOI:10.1021/acscatal.0c04371.

(45) Biesinger, M. C.; Hart, B. R.; Polack, R.; Kobe, B. A.; Smart, R. S. C. Analysis of Mineral Surface Chemistry in Flotation Separation Using Imaging XPS. *Miner. Eng.* **2007**, *20* (2), 152–162. DOI:10.1016/j.mineng.2006.08.006.

(46) Ivanova, T. M.; Maslakov, K. I.; Sidorov, A. A.; Kiskin, M. A.; Linko, R. V.; Savilov, S. V.; Lunin, V. V.; Eremenko, I. L. XPS Detection of Unusual Cu(II) to Cu(I) Transition on the Surface of Complexes with Redox-Active Ligands. *J. Electron Spectros. Relat. Phenomena* **2020**, *238* (June 2019), 146878. DOI:10.1016/j.elspec.2019.06.010.

(47) Janvelyan, N.; Van Spronsen, M. A.; Wu, C. H.; Qi, Z.; Montemore, M. M.; Shan, J.; Zakharov, D. N.; Xu, F.; Boscoboinik, J. A.; Salmeron, M. B.; Stach, E. A.; Flyztani-Stephanopoulos, M.; Biener, J.; Friend, C. M. Stabilization of a Nanoporous NiCu Dilute Alloy Catalyst for Non-Oxidative Ethanol Dehydrogenation. *Catal. Sci. Technol.* **2020**, *10* (15), 5207–5217. DOI:10.1039/d0cy00683a.

(48) Kumar, A.; Bal, R.; Srivastava, R. Modulation of Ru and Cu Nanoparticle Contents over CuAlPO-5 for Synergistic Enhancement in the Selective Reduction and Oxidation of Biomass-Derived Furan Based Alcohols and Carbonyls. *Catal. Sci. Technol.* **2021**, *11* (12), 4133–4148. DOI:10.1039/D1CY00593F.